Project Title:

NeTS: Small: RUI: Bulldog Mote- Low Power Sensor Node and design Methodologies for Wireless Sensor Networks

Energy Harvesting Technologies

PD/PI Name:

Nan Wang, Principal Investigator

Woonki Na, Co-Principal Investigator: Lead Energy Harvesting Team

Recipient Organization:

California State University-Fresno Foundation

Team Members:

Maen Marji,Cheaheng Lim, and Honorio Martinez

Project/Grant Period:

10/01/2018 - 09/30/2021(no cost extension to 03/31/2021)

Reporting Period:

10/01/2020 - 09/30/2021

Signature of Submitting Official (signature shall by submitted in accordance with agency specific instructions):

ABSTRACT

This report is for the energy harvesting activities in the project, 2020~2021. During 2020~2021, a multi-source Energy harvester for low power applications have been studied explicitly. Solar and wind energy are extracted to supply a wireless sensor and charge a single-cell Li-ion battery. The maximum power point tracking (MPPT) technique implemented using DC-DC Converters for high-efficiency harvesting. Additionally, the proposed CC/CV battery charging algorithm was established based on the renewable source's maximum power availability. At the same time, the Vibration energy harvested using Piezoelectric strings is stored temporarily in a capacitor then discharged into the DC bus or directly to the load through a DC-DC converter to provide more stability to the system responses. Also, multiple control techniques have been developed, such as a linear controller (PI), a combination of linear and non-linear controllers (PI and Hysteresis switching control), and Fuzzy logic controller (FLC). Then a comparison between each controller was observed in both simulation and experimentally for MPPT and CC/CV battery charging. The multi-source energy harvester was implemented on an SMD PCB circuit prototype. Similarly, the Hysteresis switching control (HSC) was implemented as a mixed-signal design using SMD PCB.

Table of Contents

Table of Figures

List of Tables

Chapter One: Multi-Source Renewable Energy Harvesting for Low Power Applications.

1.1 Introduction

Rapid technological change has increased the demand for the use of renewable energy. Besides, the need to find new ways to extract energy from the surrounding environment becomes imperative. Therefore, many methods have been developed to improve renewable energy harvesting, such as solar, wind, thermal, vibration, etc. Hence, solar and wind energy are considered macro energy harvesting, while thermal and vibration are considered micro energy harvesting. However, solar and wind can still be used in low power applications such as supplying power to wireless sensors, medical sensors, and radio transmitters. Thus, this research is focused on the methods of harvesting these low energies at maximum efficiency, then store it properly.

Starting with the full understanding of renewable sources models and how to extract the maximum power using DC-DC converters, then increasing the efficiency to store this energy is the main topic in this research. The overall system topology shown in Fig. 1 contains a photovoltaic panel, wind turbine, piezoelectric string, and power stage for each energy source. Buck-boost for the solar panel and buck converter for both wind and piezoelectric sources. Also, a battery and wireless sensor are used as a load. Controller and power management generate the control signals required to maintain the system stability, efficiency, and protection by monitor and sense all the system components. Therefore, the first section of this research focuses on designing different control methods for energy harvesting using MPPT. Secondly, charging the Li-ion battery using CC/CV based on the MP available.

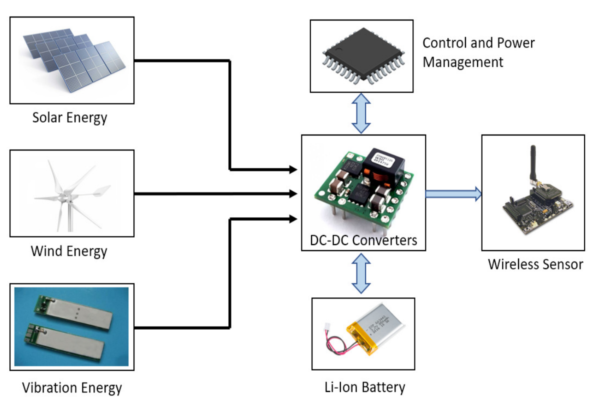

Figure 1.1: Energy harvester for wireless sensor.

This section discusses the methods of harvesting and controls renewable energy sources for low power applications. Linear controller, non-linear controller, and combination of both have been developed, where the results are compared in simulation and experimentally. Finally, Hardware implementation has been done on PCB design using surface mount technology to reduce the size and increase efficiency.

1.2 Renewable Energy Sources

1.2.1 Solar Energy Harvesting

Solar panels are made from a combination of photovoltaic cells made mainly of silicon connected in series and parallel to produce the required voltage and current. Each cell is two layers of a semiconductor material doped differently in a way that forms a P-N junction, as shown in Fig 1.2 that represents the solar cell structure. In other word, the solar cell could be presented as a shunt diode with a series and parallel resistors. The structure is made to absorb the photons that are carried in the solar irradiance making the electrons leave their atoms, producing a negative charge in the top layer (n-type silicon) and positive charge (holes) in the thicker bottom layer (p-type silicon). Eventually, when there is enough irradiance absorbed by the cell, a potential difference between the two layers causing the electrons to flow from the N-junction to the P-junction, forming a current flowing from the positive terminal to the negative terminal of the solar cell. The capacity of absorption is affected by the structure of the PV cell. An anti-reflective coating layer is added to the surface of the PV cell to enhance the capacity of absorption. An intrinsic layer is also added to extend carriers' lifetime, increasing the optically produced electron-hole [30]. More details about solar cell structure can be found in [31].

Equation (1.1) and (1.2) represent ideal and practical equations of I-V characterization of PV cell [5]. Fig. 1.3 shows the equivalent circuit of the ideal and practical photovoltaic cell [1]. Where the parameters are: I_d: the diode current, I_{ph}: the photo voltaic current, R_s: The series resistance is the internal Ohmic resistance of the PV cell, R_p: The parallel resistance represents the stray currents such as leakage and recombination currents.

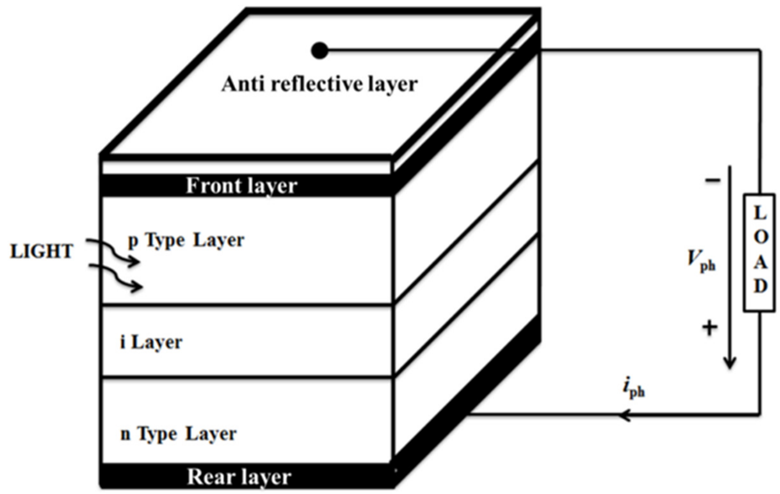

Figure1.2: Basic structure of the PV cell [43].

$$I = I_{pv,cell} - I_{o,cell} \left[\exp\left(\frac{qV}{akT}\right) - 1\right] \tag{1.1}$$

$$I = I_{ph} - I_o \left[\exp\left(\frac{V + R_s I}{V_t a}\right) - 1\right] - \frac{V + R_s I}{Rp} \tag{1.2}$$

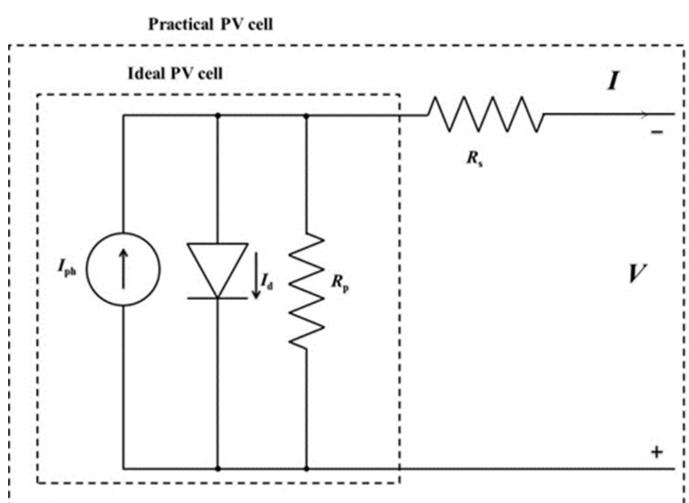

Figure 1.3: The equivalent circuit of the practical photovoltaic cell [1].

The PV cell's output efficiency could be affected by many factors such as irradiance, temperature, load impedance, and the internal structure of the cell. Where sunlight can provide around 100 mW/Cm^2 and with cloudy day, it can deliver 1/10 of that power [2]. In contrast, the solar cell efficiency can convert this power with maximum efficiency up to 50% for space-grade PV cells while up to 20% for conventional ones. Also, getting that efficiency to its maximum value, the PV cell equivalent impedance must match the load impedance as close as possible to guarantee maximum power transfer from the PV cell to the load. Besides, this is due to the characteristics of the PV cell, where the current and voltage curve of the PV cell shown in Fig. 1.4 is the result of changing the load from open circuit to short circuit. The maximum current output happens at the short circuit between the positive and the negative terminals of the solar cell, where this current is called the short circuit current (Isc). The maximum output voltage happens at an open circuit, and it is called Open circuit voltage (Voc).

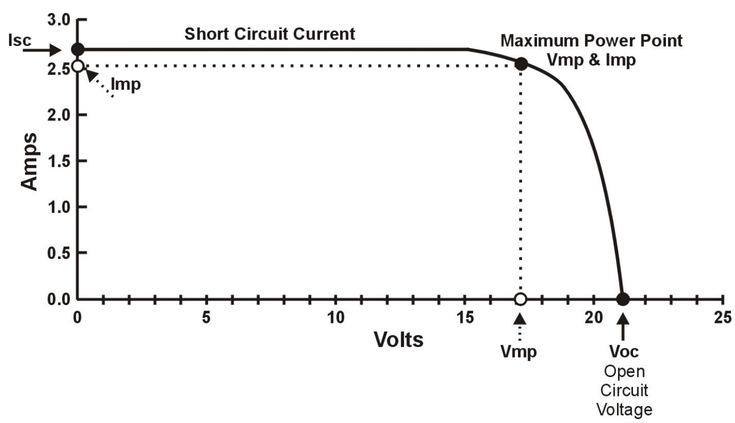

Figure 1.4: I-V Characteristic curve of PV module [3].

From the I-V curve, it can be noticed that there is a point slightly less than the short circuit current and the open-circuit voltage called the maximum power point (MPP) located at the knee of the curve. The P-V carve clarifies that point at the top of the hill, as shown in Fig. 1.5. The MPP happens when the load impedance becomes close to the PV cell impedance, as mentioned previously. Tracking this point is significant for optimum harvesting. Therefore, many maximum power point tracking algorithms have been developed, such as Perturb & Observe, Incremental Conductance, Fractional Open-Circuit Voltage, and Fractional Short-Circuit Current. Also, different control techniques are used as well to track MPPT based on the previous algorithms, such as Sliding Mode Control, Fuzzy logic, Kalman Filtering, Artificial Neural Networks, and Optimization Algorithms. These methods will be discussed in more detail in sec 1.4.

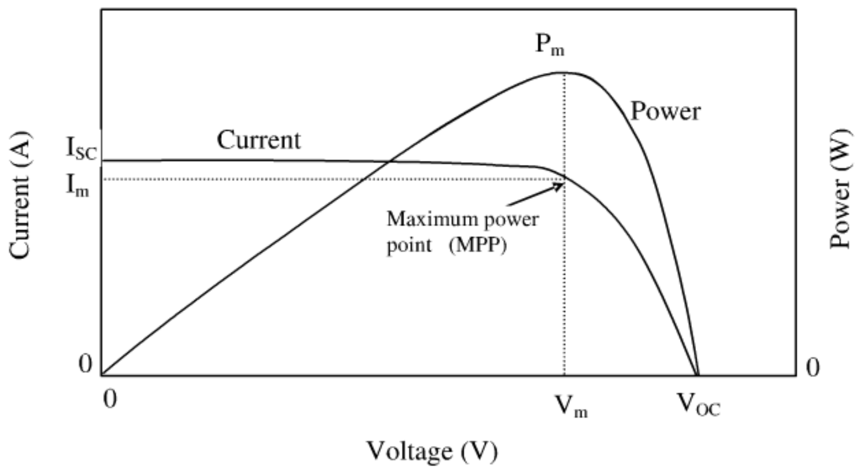

Figure 1.5: PV & IV curve for PV cell [4].

At last, there are many structural shapes for PV cells, such as monocrystalline and polycrystalline. In this project, a monocrystalline was chosen due to the higher efficiency between 15-20% compared to polycrystalline with average efficiency between 11-16%. Connecting these cells in series and parallel forms PV Module or panel. Also, connecting panels in series and parallel forms PV array, where large array or multiple of arrays called Solar farm as shown in Fig. 1.6. the connection of series increases the output voltage of the panel while connecting in parallel increase the produced current based on Kirchhoff's voltage & Current Laws (KVL & KCL).

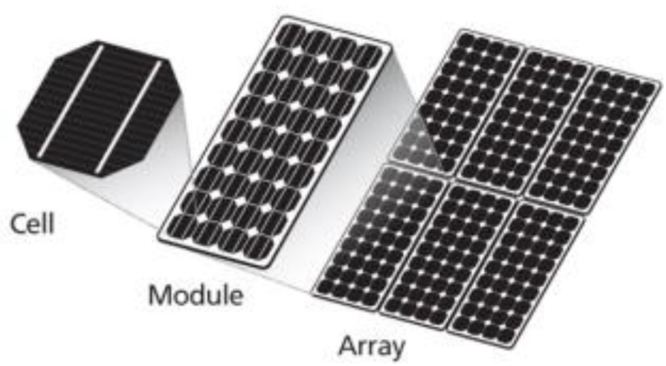

Figure 1.6: Array and Module Structure starting from single PV cell [38].

1.2.2 Wind Energy Harvesting

Wind energy harvesting is one of the most common renewable energy harvested so far due to its wide range of applications, where it can vary by size and power rating from tens of watts to few megawatts [5]. Therefore, wind energy harvesting is the process of converting wind energy into electricity. This conversion is done using wind turbines that absorb the wind energy and convert it into rotational energy using blades that rotate a DC or AC electrical generator's shaft. However, this process is much more complicated and requires unique control systems in both mechanical and electrical sides. This report will discuss the mechanical system of wind energy conversion concept lightly, while it will discuss the depth of how to extract the maximum power from a PMDC generator based on the motor shaft speed.

A modern wind turbine single line diagram is shown in Fig 1.7. it can be noticed that the wind turbine converts the wind energy into rotational energy (Both are Kinetic energy), which rotates a shaft. Then, the speed and the torque are controlled using either an automated or regular gearbox to adjust the voltage and frequency in case of AC generation. Also, in AC generation, the AC power is converted into DC to apply MPPT and adjust the voltage level, then converted back into AC to be fed to the grid.

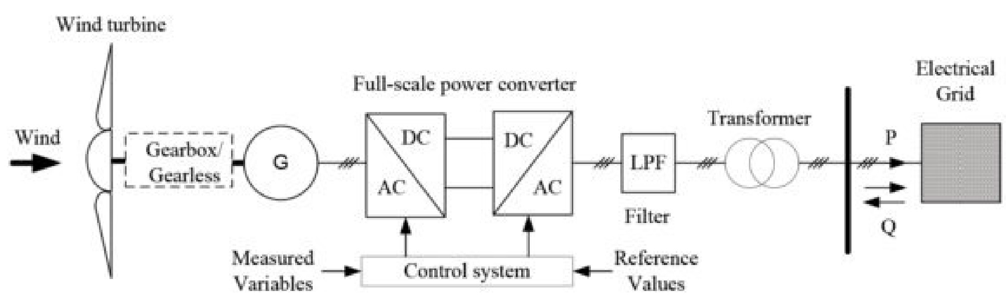

Figure 1.7: Typical fully rated converter coupled wind turbine generator [6].

However, in some applications, the DC generation method is more convenient and efficient, such as offshore wind farms and micro wind energy harvesting. The DC generation single line diagram is shown in Fig. 1.8. The DC generator shaft can be connected directly to the wind turbine in tiny turbines. Then, the generated power is fed into a DC to DC converter to extract the maximum power from the wind turbine by changing the duty cycle of the converter.

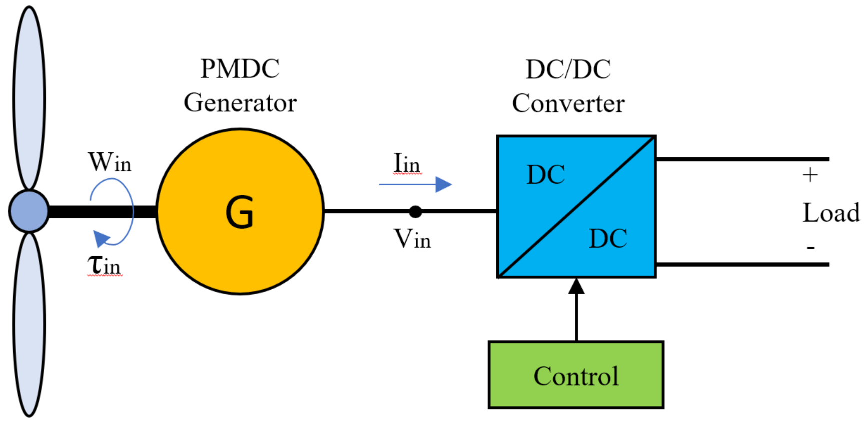

Figure 1.8: Single line diagrams of DC wind generator connected to a DC/DC Converter.

The wind power conversion equation is [7]:

$$P = 0.5\rho A C_p V^3 N_g N_b \tag{1.3}$$

Where ρ is the air density in Kg/$m3$, A is the rotor swept area in $m2$ where it can be calculated using equation (1.4), Cp is the coefficient of performance (Power Coefficient), V is the wind velocity (m/s), Ng is the generator efficiency, and Nb is the gearbox bearing efficiency. However, this application does not have a gearbox, and the value of Nb is one, and Ng depends on the generator structure.

$$A = \pi R^2 \tag{1.4}$$

R is the turbine blade radius.

In addition, the power coefficient C_p depends on the pitch angle of the blade, and the tip speed ratio(λ), that can be calculated using equation (1.5). The tip speed ratio achieves optimal value at optimal wind speed. Thus, from equations (1.3 & 1.5) the optimal or maximum power conversion achieved at the optimal shaft speed [8]. Thus, the relation between the wind speed, turbine speed, and turbine output power can be represented in Fig. 1.9.

$$\lambda = \frac{\omega R}{V_\omega} \tag{1.5}$$

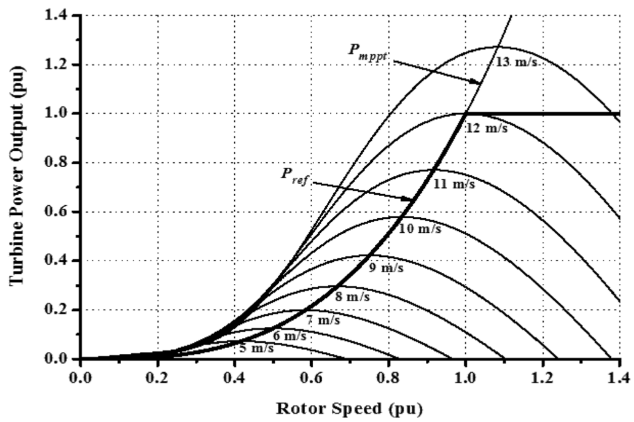

Figure 1.9: The characteristic curve of a wind turbine [40].

The power converted from the wind turbine represents the input power for the permanent magnet DC generator as a mechanical torque and angular velocity on the shaft. The DC generator consists of a field circuit, which is a permanent magnet in PMDC generators. It also contains the armature circuit with the copper windings and the commutator that rectifies the generated voltage into a DC power using brushes. The equivalent circuit of a DC generator is shown in Fig. 1.10. Consequently, the relation between the mechanical input power and the electrical output power is:

$$P_{out} = P_{conv} - P_{copper} - P_{brushes} = V_t I_a \tag{1.6}$$

P_{conv} is the mechanical power that converted into an electromagnetic field, P_{copper} is the copper losses due to the winding resistance, $P_{brushes}$ is the brushes losses, V_t is the terminal voltage, and I_a is the armature current. Therefore, the electromechanical conversion equation is:

$$P_{conv} = \omega_m \tau_m = \omega_m \tau_e = P_{in} - P_{stray} - P_{f\&W} - P_{core} \tag{1.7}$$

$$P_{conv} = E_a I_a \tag{1.8}$$

$$E_a = K\varphi\omega_m \tag{1.9}$$

ω_m: Motor shaft angular velocity (rad/s).

τ_m: Mechanical torque delivered by the motor shaft (N.m).

τ_e: The electromagnetic torque in the airgap between the rotor and the armature (N.m)

P_{in}: The input power in watt

P_{stray}: The stray losses of the DC generator in watt

$P_{f\&W}$: The friction and windage losses in watt

P_{core}: Core losses due to the core reluctance in watt.

E_a: The induced voltage (volt)

K: Constant related to the construction of the DC generator

φ: The induced flux in the airgap and the iron core Volt.S/rad

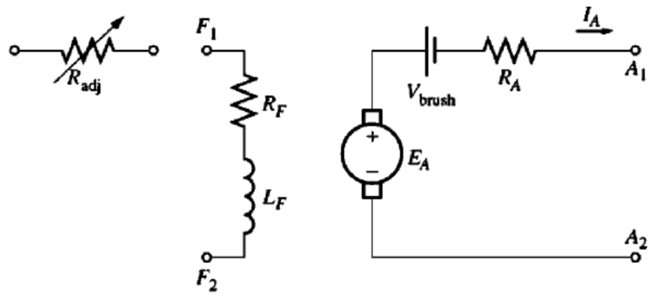

Figure 1.10: The equivalent circuit of a DC generator [44].

1.2.3 Vibration Energy & Piezoelectric Material

The small amount of Vibration energy harvesting is accomplished using crystalline material called Piezoelectric material. The use of this material is widely used as sensors, speakers, and micro energy harvesters. Thus, this material is used in a vast number of applications in almost all fields such as medical, military, sports, traffic engineering, automation, and industrial fields. The material converts the mechanical stresses into electricity in a process called the Piezoelectric effect. This effect was discovered for the first time in 1880 by Jacques and Pierre Curie during their studies of the effect of pressure to generate electrical charges by quartz [9]. Thus, the piezoelectric generator modeling and simulation was studied in this project report.

The piezoelectric material could have many forms depending on the application. In this project, the string shape was chosen to allow harvesting vibration from the environment. The crystalline material that forms the piezoelectric string has symmetric charge distribution at rest (no stress applied). Thus, the symmetric charge distribution makes the electric dipole moments equal to zero, as shown in Fig. 1.11. Although, when mechanical stress is applied, the charge will be no longer symmetric, and the dipole polarization will be created, causing to build a voltage difference between the two plates that sandwich the piezoelectric material [9]. Thus, the vibration energy will cause net polarization to change internally, creating a voltage difference with a frequency depending on the vibration level.

To achieve maximum energy harvesting, the frequency must always be much less than the piezoelectric material's resonant frequency. Therefore, it can be represented as a parallel plate capacitor. Also, the converted electric energy using a piezoelectric element that has surface area S, thickness t, and loaded with stress σ can be found by [10]:

$$U = \frac{1}{2} QV = \frac{1}{2} (d \times \sigma \times S) \cdot (g \times \sigma \times t) \tag{1.10}$$

Where d is the current constant, and g is the voltage constant.

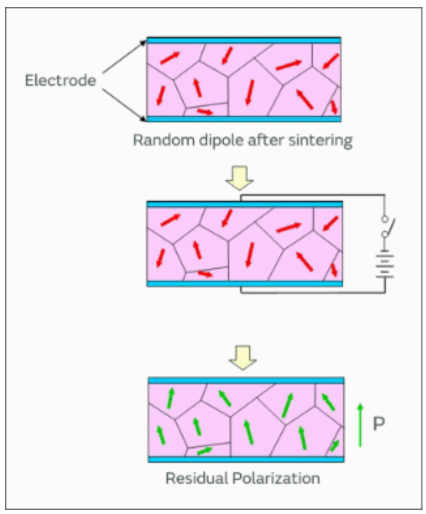

Figure 1.11: Polycrystal Polarization due to piezoelectric effect [11].

There is multiple developed spice model or equivalent circuit of the piezoelectric strings based on the characteristic of the piezoelectric effect. The main two models can be shown in Figs 1.12-1.13. The first model has been developed by Mouapi and Hakem [12], while the second model was represented in [13]. Both models can be simulated in Spice or Simulink software, where the second model fits the piezoelectric string for energy harvesting.

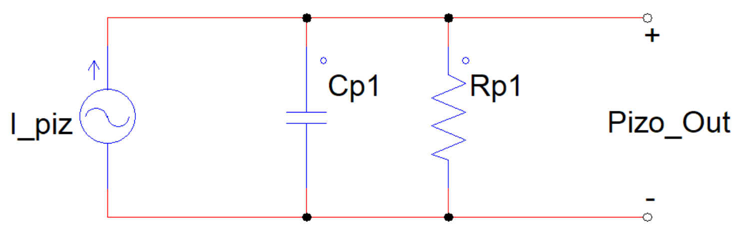

Figure 1.12: Parallel model of the Piezoelectric transducer using sinusoidal current source.

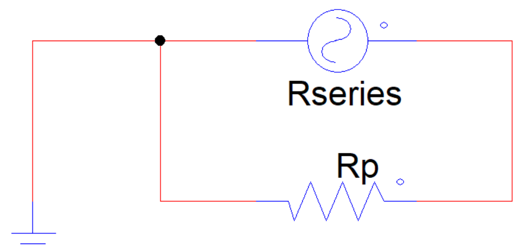

Figure 1.13: Voltage Source model of piezoelectric transducer [13].

1.3 DC/DC Converters.

DC-DC converters are a DC level shifter that changes the input voltage from one level to another using switching and filter topology. The most common DC-DC converters are the buck, Boost, and Buck-Boost converters. In this report, the buck and boost converters are studied in detail, including the average modeling.

The buck is used to step down the voltage by controlling the switch and reduce the input voltage by a factor equal to the duty cycle, while the boost converter is used to step up the voltage. However, the switch is controlled by sending a control signal from the controller to the PWM generator that drives the gate of the switch. Fig. 1.14 is a buck while Fig. 1.15 is a boost converter. Accordingly, the two circuits could be compound using one inductor and output capacitor to form a buck-boost circuit, as shown in Fig. 1.16. The advantage of using this circuit model for the buck-boost is that the output is not inverted like in the regular buck-boost circuit shown in Fig. 1.17.

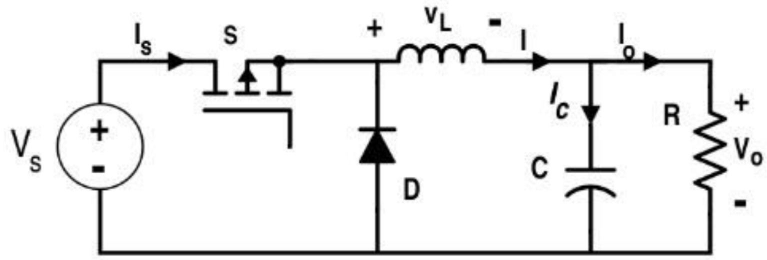

Figure 1.14: Buck converter circuit [39].

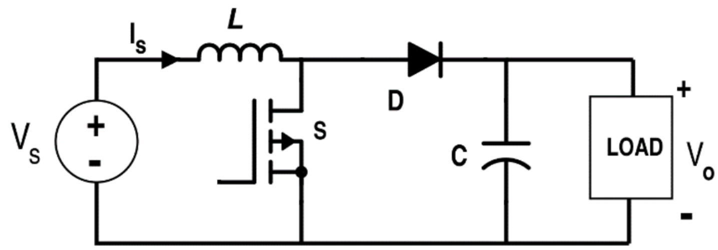

Figure 1.15: Boost converter circuit [39].

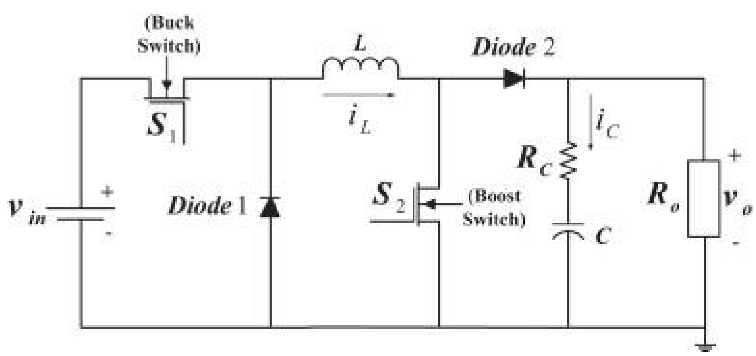

Figure 1.16: 2-Switch non-inverting Buck-Boost converter circuit [39].

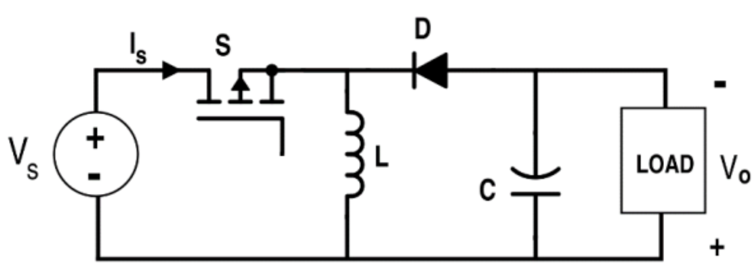

Figure 1.17: Inverting Buck-Boost converter circuit [39].

The Buck converter circuit consists of a switch, diode, and an LC filter. The switch is responsible for reducing the voltage level (step down) to the desired value controlled by the pulse width modulated signal's duty cycle, as shown in Fig. 1.18. Equation (1.11) is the output voltage and duty cycle relationship, while Eqs. (1.12-1.14) are the equations of the output current, inductor ripple current.

$$V_{out} = DV_{in} \tag{1.11}$$

$$I_L = I_o = \frac{V_{out}}{R} \tag{1.12}$$

$$\Delta i_L = \frac{V_{in} - V_{out}}{L} DT_s \tag{1.13}$$

$$I_{in} = DI_L = DI_{out} \tag{1.14}$$

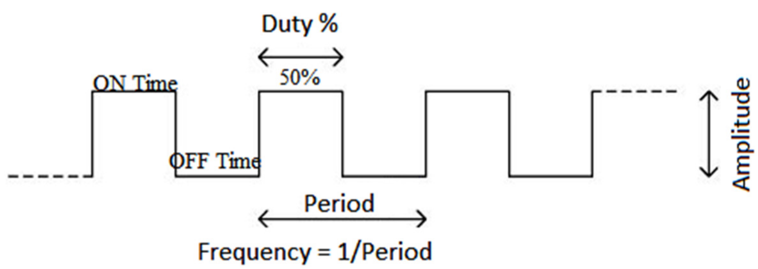

Figure 1.18: Pulse Width modulation signal with 50% duty cycle [14].

Furthermore, the DC-DC converters' design depends on many factors such as the input voltage, the desired output voltage, the maximum current, the desired output ripple, and the load type. Thus, to find the values of L and C in the buck converter, Eqs. 1.15-1.16 are used [15]:

$$L = \frac{V_{out} \times (V_{in} - V_{out})}{\Delta I_L \times f_s \times V_{in}} \tag{1.15}$$

$$C_{out} = \frac{\Delta I_L}{8 \times f_s \times \Delta V_{out}} \tag{1.16}$$

Where:

$Cout$: Minimum output capacitance

ΔI_L: Inductor ripple

f_s: Minimum switching frequency

ΔV_{out}: Desired output voltage ripple

Consequently, Boost Converter is a DC to DC converter that steps up the voltage from low value to higher desired value by controlling the PWM signal's duty cycle. Eqs (1.17-1.19) is the output voltage, output current, and inductor ripple current.

$$V_{out} = V_{in} \frac{1}{1-D} \tag{1.17}$$

$$I_L = I_{in} = \frac{I_{out}}{1-D} = \frac{1}{1-D}\frac{V_{out}}{R} \tag{1.18}$$

$$\Delta i_L = \frac{V_{in}}{L} DT_s = \frac{V_{out} - Vin}{L}(1-D)T_s \tag{1.19}$$

Also, Eqs (1.20-1.21) is the equations used to calculate the L and C value based on design specification [16].

$$L = \frac{V_{in} \times (V_{out} - V_{in})}{\Delta I_L \times f_s \times V_{out}} \tag{1.20}$$

$$C_{out} = \frac{I_{out} \times D}{f_s \times \Delta V_{out}} \tag{1.21}$$

Eventually, the 2-switch noninverting buck-boost converter has the output-input relationship shown in Eq (1.22). The converter transition will depend on the values of d1 and d2 based on the input voltage at constant output voltage or vice versa. Also, the 2-switch buck-boost converter's circuit allows it to work either in buck mode or boost mode only. Therefore, if switch two is kept OFF and controls the duty cycle of switch one, the converter will work as a buck only. On the other hand, if switch one kept ON continuously with controlling the duty cycle on switch two, the converter will work as a boost converter only.

$$V_{out} = V_{in} \frac{d_1}{1-d_2} \tag{1.22}$$

Where d_1 is the duty cycle of switch one, and d_2 is the duty cycle of switch two. Also, for calculating the values of L and C, the following constraints must be taken into consideration [17]:

Inductor value in the buck mode:

$$L > \frac{V_{out} \times (V_{INmax} - V_{out})}{K_{ind} \times F_{sw} \times V_{INmax} \times I_{out}} \tag{1.23}$$

Inductor Value in boost mode:

$$L > \frac{V_{INmin}^2 \times (V_{out} - V_{INmin})}{K_{ind} \times F_{sw} \times I_{out} \times V_{out}^2} \tag{1.24}$$

Capacitor value in buck mode:

$$C_{out} = \frac{K_{ind} \times I_{out}}{8 \times F_{sw} \times V_{ouTripple}} \tag{1.25}$$

Capacitor value in boost mode:

$$C_{out} = \frac{I_{out} \times D_{boost}}{F_{sw} \times \Delta V_{ouT}} \tag{1.26}$$

K_{ind} is an estimated coefficient that represents the amount of inductor ripple current relative to the maximum output current.

1.4 Maximum Power Tracking Techniques For renewable energy harvesting.

The maximum power point tracking is a technique used to extract the maximum power available in the photovoltaic cells or the wind turbines. It could also be applied to other renewable sources such as vibration and thermal energy harvesting since most renewable sources are nonlinear sources in nature; whether it is considered current or voltage sources, the output power will depend on many factors. These factors are mainly limited to the temperature and irradiance in solar energy harnessing, while the wind speed and the pitch angle are the main factors that effects wind energy harvesting. Besides, connecting a load to such sources causes an un-matching problem with the source, which leads to extracting less power than the sources' capability. However, this issue is solved using many algorithms that keep tracking the renewable source's maximum power point by connecting a fully controlled mediator, which is mainly power electronic circuits that controlled using switches such as IGBTs or MOSFETs. Therefore, the MPPT algorithm is an analog or digital technique that allows the PV to operate at MPP at any environmental condition [18].

The Perturb and Observe (P&O) method is commonly used due to its simplicity and ease of implementation [32]. The output voltage (V) and output current (I) of the renewable module are sensed. Then power is calculated (Pn) and compared with the previous value (Pn-1) to calculate ΔP. According to the sign of ΔP and ΔV, the MPP is tracked. If the ΔP positive thus there is an increment in power, the perturbation should be kept in the same direction. On the other hand, if it is negative, the next perturbation should be in the opposite direction. These processes are repeated until the MPP is reached. Therefore, the operating point is oscillating around MPP. This method becomes unstable, with a change in environmental conditions [19].

The second method is the incremental conductance algorithm, which is faster and more robust in finding the MPP. The incremental conductance method based on the fact that the slope of the PV module power curve is zero at MPP, negative on the right and positive on the left.as given in the flow chart shown in Fig 1.20 [19-20].

$$\begin{aligned} \frac{dp}{dv} &= 0, \ \ at\ MPP \\ \frac{dp}{dv} &> 0, \ \ left\ of\ MPP \\ \frac{dp}{dv} &< 0, \ \ right\ of\ MPP \end{aligned} \tag{1.27}$$

Since:

$$\frac{dP}{dV} = \frac{d(IV)}{dV} = I + V\frac{dI}{dV} \cong I + V\frac{\Delta I}{\Delta V} \tag{1.28}$$

Also, Eqs. (3) Can be written as:

$$\begin{aligned} \frac{\Delta I}{\Delta V} &= -\frac{I}{V}, \qquad at\ MPP \\ \frac{\Delta I}{\Delta V} &> -\frac{I}{V}, \qquad left\ of\ MPP \\ \frac{\Delta I}{\Delta V} &< -\frac{I}{V}, \qquad right\ of\ MPP \end{aligned} \tag{1.29}$$

This method's operation is summarized by measuring the present value of voltage (Vpv) and current (Ipv), then calculate the incremental change ΔI and ΔV using present and past values of voltage and current. Accordingly, by comparing the instantaneous conductance (I/V) to the incremental conductance (ΔI/ΔV), the MPP is tracked. If the ΔI/ΔV > -I/V, the operating point at the MPP's left side must be moved to the right by increasing voltage. On the other hand, if $\Delta I/\Delta V < -I/V$, the operating point at the right side of the MPP must be moved to the left by decreasing voltage. If $\Delta I/\Delta V = -I/V$, the MPP is reached [19]. The INC algorithm flowchart is shown in Fig. 1.9

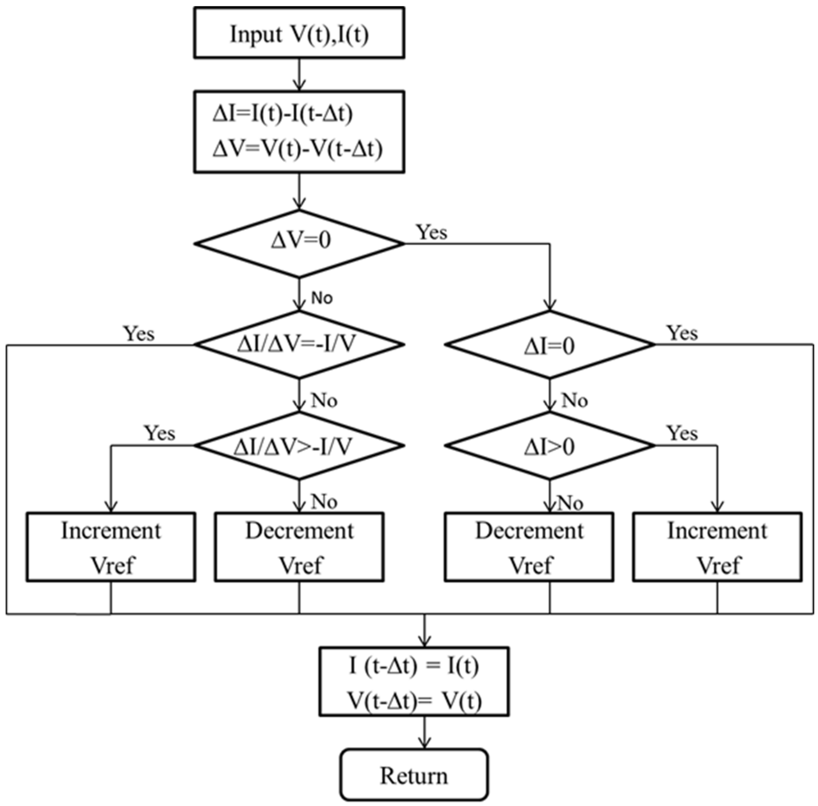

Figure 1.19: Flowchart of INC MPPT technique [45].

1.5 Li-Ion Battery Model & Charging Techniques.

Li-ion batteries are widely used in electric vehicles due to their high energy density, high safety level, long cycle life, and durability. However, charging a li-ion battery requires very regime charging techniques. Thus, a full understanding of li-ion battery construction is important to apply the optimum method for safe charging.

Single-cell Li-Ion batteries are made mainly from a negative electrode, positive electrode, and electrolyte. The negative electrode is made from carbon, while the positive electrode is a metal oxide. Also, the electrolyte is a lithium salt in the organic solvent [21]. This electrolyte is highly flammable, which excessive charging will lead to a fire hazard. Thus, a long trickle charging technique is not recommended compared to conventional lead-acid batteries.

The first order RC equivalent charging circuit for a single-cell Li-ion battery is shown in Fig. 1.20.1 [22-23]. Rr is the series internal resistance of the battery, Rp and Cp are the polarization capacitance and resistance, respectively, OCV is the open-circuit voltage, U_o is the terminal voltage, and I_{charge} is the charging current. Thus, from the equivalent model, the following equations can be obtained as following [22-23]:

$$C_p \frac{du_p(t)}{dt} + \frac{u_p(t)}{R_p} = i(t) \tag{1.30}$$

$$u_o(t) = u_{ocv(t)} + i(t)R_r + u_p(t) \tag{1.31}$$

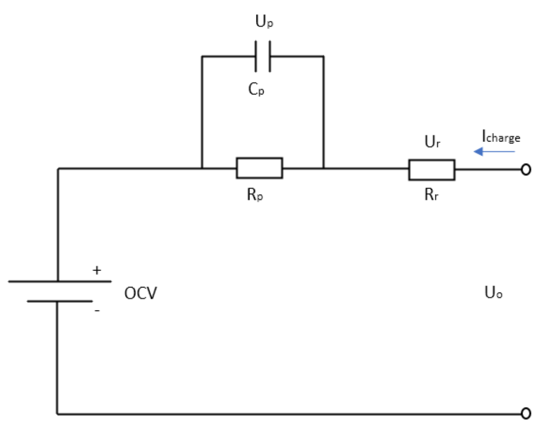

Figure 1.20 First order RC equivalent charging circuit of Li-ion battery [22-23].

The mathematical battery model is numerically solved using the software package COMSOL Multiphysics V5.4. A classic pseudo 2D approach was used[46], where a one-dimensional battery model and a two-dimensional electrode solid phase model. The battery charge or discharge operation from fully discharged state or fully charged state is firstly simulated at constate C-rate applied, which strictly followed our experimental procedure. Similarly, the EIS simulation then is carried out by applying a voltage perturbation of 5mV in amplitude with frequency ranging from 10mHz to 10kHz on the positive NMC electrode current collector surface, which also strictly followed the same protocols as our experimental EIS tests. The simulated impedance profile can be calculated based on the current output signal. The details of the new battery model can be found in [47]. Also, there are many methods for charging Li-ion Battery. Table 1.1 shows all the available algorithms used to charge li-ion battery [24]. However, the only algorithm tested in this report is the CC/CV algorithm due to its simplicity and ease of implementation. Also, it can be implemented as an analog or digital controller. The flowchart for the CC/CV algorithm is shown in Fig. 1.21. Based on the algorithm, the li-ion battery will start charging using a constant current at 1C or less until the battery voltage reaches the cut-off voltage. After that, the battery will charge in constant voltage at the cut-off voltage until the current is reached 0.1C. 1C represents the rated capacity of the Li-ion battery. Fig. 1.22 represent the charging profile for the CC/CV method.

TABLE 1.1: MAJOR CHARACTERISTICS OF CHARGING ALGORITHMS [24].

Charging Algorithm	**Analog or Digital**	**Charging Time**	**Charging Efficiency**	**Implementation complexity**	**Cycle Life**	**Sensed Parameter**
CC/CV	Both	L	L	M	L	V, I, T
DL-CC/CV	Analog	L	L	L	L	V, T
BC-CC/CV	Both	H	L	M	L	V, I, T
FL-CC/CV	Digital	M	M	H	M	V, I, T
GP-CC/CV	Digital	M	M	H	M	V, I, T
PLL-CC/CV	Analog	L	M	M	L	V, I, T
IPLL-CC/CV	Analog	L	M	M	M	V, I, T
MSCC	Digital	M	M	H	M	V, I, T
FCV-PC	Digital	H	H	H	H	V, I, T
DCV-PC	Digital	H	H	H	H	V, I, T
CC-PC	Digital	H	H	H	H	V, I, T

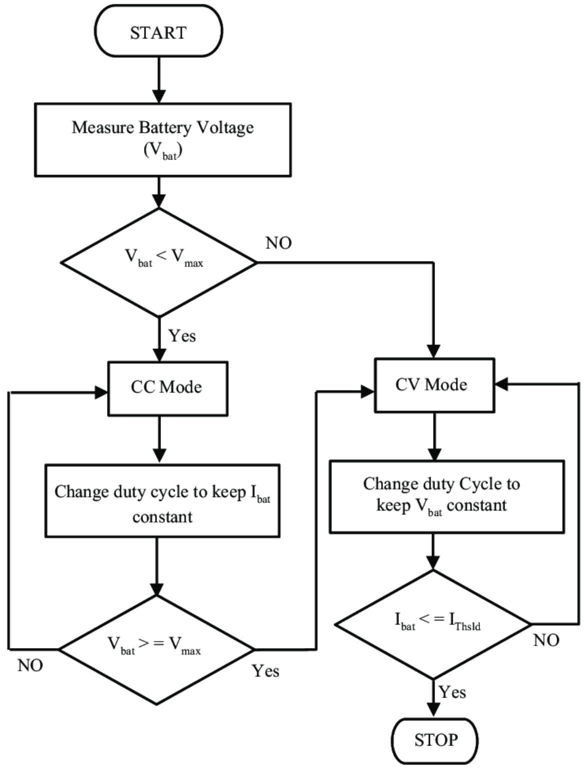

Figure 1.21: Flowchart for the CC/CV algorithm [24].

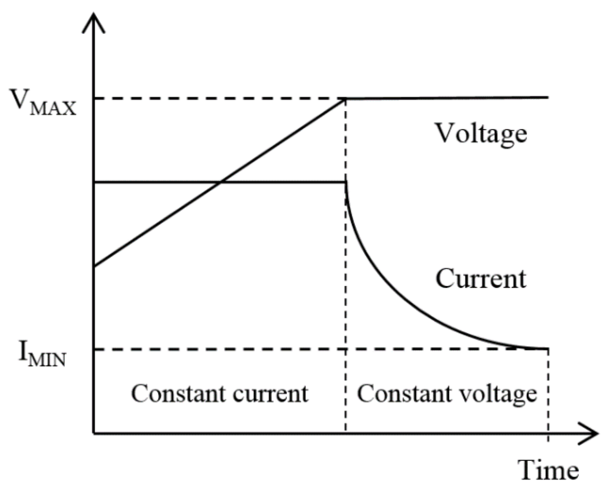

Figure 1.22: Charging profile for CC/CV algorithm [25].

Following one of these algorithms for charging a li-ion battery is essential to increase the battery's lifetime and protect it from overvoltage and overcurrent charging. Also, it keeps the internal temperature at the rated values during charging, which protects the battery from turned on fire. The battery used in this project is a 3.7-volt single-cell Li-ion battery with 350mA rated capacity. Based on the manufacturer, the charging cutoff voltage is 4.2 volt, while the discharging cutoff voltage is 3 V. the full charge voltage is 4.5 volt where this value depends on many factors such as the age, and the ambient temperature.

1.6 Linear & Non-Linear control

1.6.1 Linear Controller and Linear Average Modelling

A Linear system is a system that is represented using linear differential equations. Thus, linear modeling does not consider the nonlinearities in the system, such as saturation and non-uniform characteristics. However, a linear controller will be designed based on the plant or the model of the system. Fig 1.23 shows a closed-loop linear control system, in which feedback from the output is compared to the desired value. Then, using a linear controller (compensator), the error is eliminated by adjusting the system's input. System limitations and modeling accuracy constrain this process.

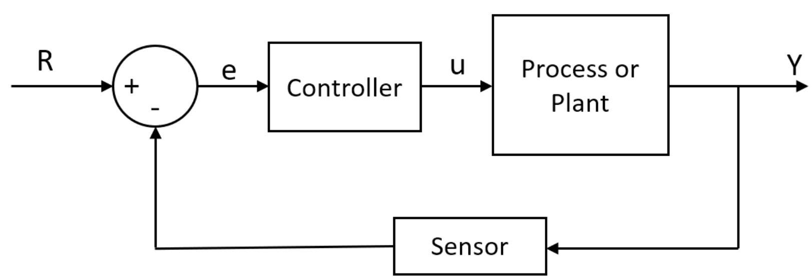

Figure 1.23: Linear Control System [42].

In this report, the average modeling or state-space modeling of buck, boost, and buck-boost converters are investigated. The DC-DC converters are nonlinear systems due to the switching elements such as MOSFETs and IGBTs. Nevertheless, the superposition rule can be applied to different states of the system. Thus, an average model can be formulated through the switching period as two sets of linear differential equations called state-space equations. Formulating the equations requires a full understanding of the small-signal and the system's (the converter) steady-state analysis. For more details, refer to appendix B in Hart. D book for power electronics [26]

The transfer function can be derived from the state-space equations. Therefore, the transfer function can be easily used to design a linear controller using the root locus or bode plot method. The output voltage transfer function in the Laplace domain for the buck converter is [26]:

$$\frac{\widetilde{V_o}(s)}{\tilde{d}(s)} = \frac{V_{in}}{LC}\left[\frac{1 + Sr_C C}{S^2 + S(1/RC + r_C/L) + 1/LC}\right] \tag{1.32}$$

r_C: the equivalent series resistance (ESR) of the output capacitance

$\tilde{d}(s)$: The small signal duty cycle

For the boost converter, the output voltage transfer function is:

$$\frac{\widetilde{V_o}(s)}{\tilde{d}(s)} = \frac{V_{in}}{(1-D)^2}(1 - s\frac{L_e}{R})\left[\frac{1 + Sr_C C}{L_e C(S^2 + S(1/RC + r_C/L_e) + 1/L_e C}\right] \tag{1.33}$$

Where

$$L_e = \frac{L}{(1-D)^2} \tag{1.34}$$

D: is the average duty cycle

Eqs (1.32 & 1.33) are used for designing a linear voltage controller for the buck and boost converters, respectively. On the other hand, if the current controller design is needed, Eqs (1.35 & 1.36) are used [26].

$$\frac{\widetilde{V_o}(s)}{\widetilde{i_L}(s)} = \frac{R(1 + Sr_c C)}{1 + SRC} \tag{1.35}$$

$$\frac{\widetilde{V_o}(s)}{\widetilde{i_L}(s)} = \frac{R(1-D)(1 - \frac{SL}{R(1-D)^2})(1 + Sr_c C)}{2 + SRC} \tag{1.36}$$

For Designing a linear controller such as P, PI, and PID, the bode plot analysis is required to ensure that the integrator gain can eliminate the steady-state error. Also, the design will be based on the desired overshoot percentage, response time, and settling time. These will be affected by the chosen cutoff frequency, gain margin, and phase margin. Fig. 1.24 shows the bode plot for a second-order system [27].

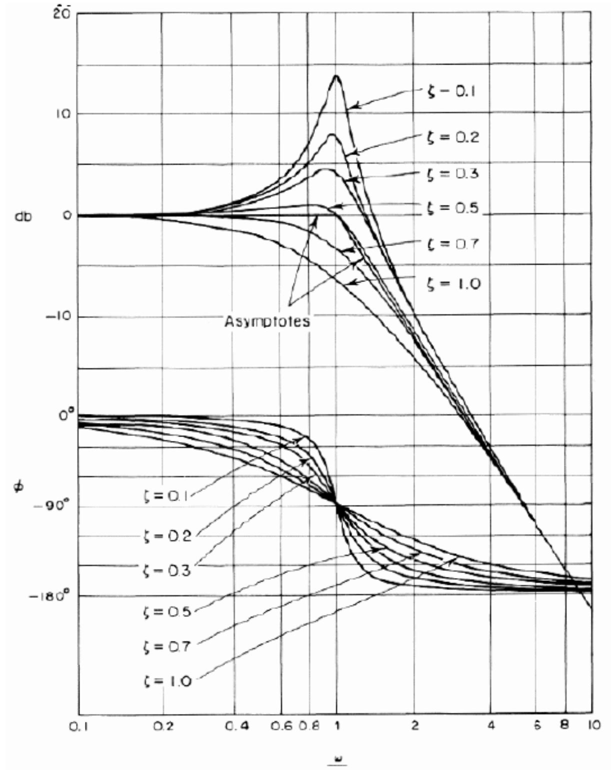

Figure 1.24: Bode plot of a second order system at different damping ratios [27].

1.6.2 Nonlinear control and phase plain trajectories.

Linear control does not take into consideration the nonlinearities in the system. Therefore, the system suffers small margin stability and robustness to large disturbances. In contrast, non-linear control is designed based on all system behaviors that lead to instability such as saturation, dead time, oscillation, backlash, and chaotic system behavior. For the better prediction of the non-linear system behavior, accurate non-linear modeling is tested extensively using simulation for a specific situation. However, multiple situations must be tested and observed. One of the techniques used to predict the behavior of the system is phase plain analysis.

The phase plane is a graphical method for studying non-linear systems. Where it shows a graph of two states versus each other as time progress. Based on the system's trajectory on the phase plane, the system instability regions and their behavior can be predicted. However, this method is limited to a system that could be represented using only three state equations (3rd order system). A general system that has the two state-space equations (1.37 & 1.38) and has the block diagram shown in Fig. 1.25 will have poles λ1, λ2 equals Eq (1.40)

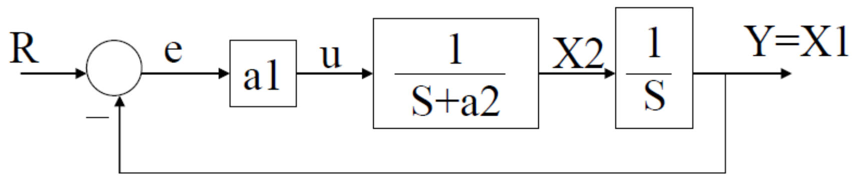

Figure 1.25: Block diagram of 2nd order system [41].

$$\dot{X}_1 = X_2 \tag{1.37}$$

$$\dot{X}_2 = -a_1X_1 - a_2X_2 \tag{1.38}$$

$$\frac{Y}{R} = \frac{a_1}{S^2 + a_2S + a_1} \tag{1.39}$$

$$\lambda_{1,2} = 0.5\{-a_2 \pm \sqrt{a_2^2 - 4a_1}\} \tag{1.40}$$

The phase plain trajectory will behave based on the location of the poles in the S-plain as shown in Fig. (1.26)

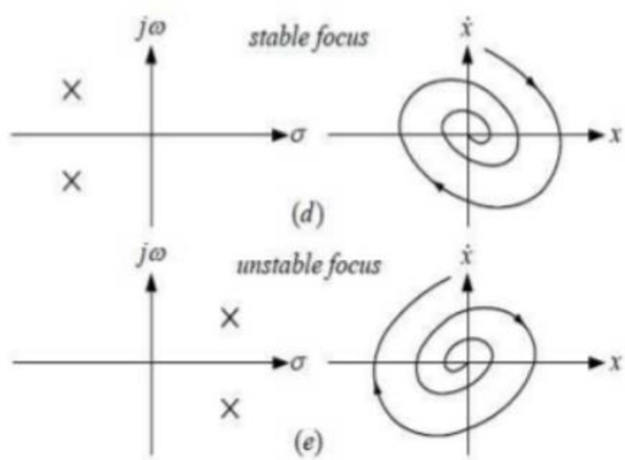

Figure 1.26: Phase plan trajectory for 2nd order system based on poles location [41].

The sliding mode control design depends mainly on the phase plane analysis to force the system to slide on the desired line or surface. On the other hand, Fuzzy logic mainly depends on the system's behavior and how the designer will need the system to react or respond to variation using linguistic conditions. Those two methods are discussed in more details in the design procedure section.

1.7 Multisource Energy Harvester and charge controller overall system.

The overall system for multi-source energy harvesting with the proposed control scheme is shown in Fig. 1.27. Three sources of renewable energy are used which solar and wind are the primary sources for the system. At the same time, the vibration energy is stored temporarily and then supplied whenever needed. Each source has its DC-DC converter designed based on the maximum available power. Also, each of these sources uses its own controller to achieve maximum power extraction and efficiency. This power will be delivered to the DC bus to be readily available to store or supply a load. Storing the energy is done using a single-cell Li-ion battery after conditioned by a bidirectional DC-DC converter. The bidirectional converter's control depends on many factors such as charging/ discharging operation, state of charge (SOC), depth of discharge (DOD), and the available power from the renewable sources. The load is a wireless sensor that works on an intermittent operation, in which the amount of energy during sleep mode is minimal, while it consumes slightly higher energy during ON time. Thus, the desired amount of power must always be delivered to the load at all conditions.

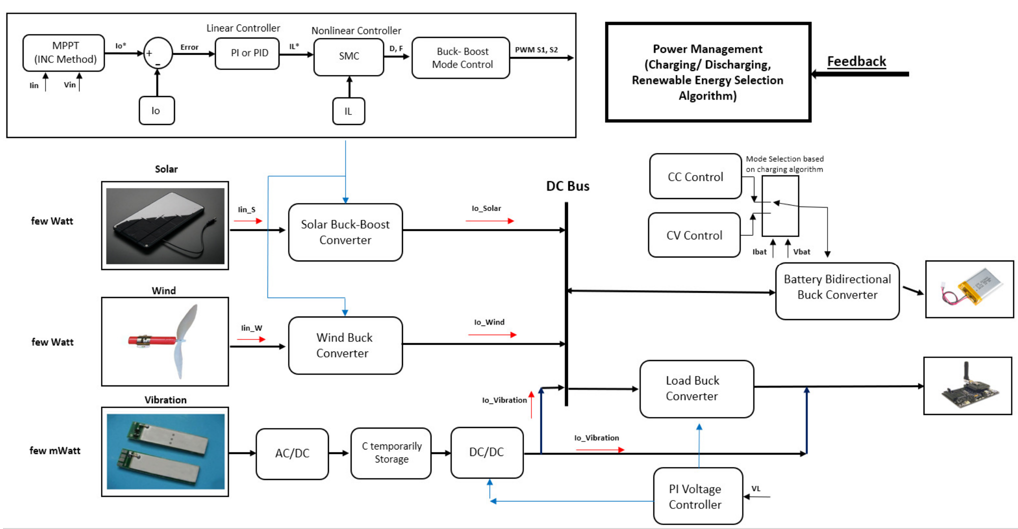

Figure 1.27: Overall system with the proposed control scheme.

Accordingly, a complete control scheme is necessary to ensure stability and maximum efficiency in the system, which is done by observing all the inputs power, output powers, and SOC of the storage device. Additionally, dropping any sources that do not have enough power, switching between charging and discharging, and system protection. All are governed by the power management algorithm shown in Fig 1.28. Moreover, from the renewable sources control scheme shown in Fig. 1.27, the MPPT algorithm finds the desired output current from the DC-DC converter based on the solar panel or the wind turbine output current and voltage (Note: input to the DC-DC converter) and then compared to the actual output current to calculate the error which fed to a linear or non-linear controller. However, in the control scheme shown in Fig 1.27, both linear and non-linear controllers are used in which the linear controller is the controller responsible for finding the desired average inductor current. Finally, the non-linear controller will create the PWM with the specific duty cycle that drives the system to have the desired inductor current, eliminating the steady-state error.

Secondly, an array of piezoelectric strings will absorb the vibration and generate an AC voltage and current. This voltage will be rectified using low power full diode bridge with an LC filter and then stored temporarily in a capacitor. After that, the stored energy will be released to the DC bus or the load. This energy stores the energy in the battery or substitutes the drop voltage when one of the renewable sources disconnected from the DC bus. A linear controller will be sufficient to drive the DC-DC converter at the desired bus or load voltage.

Third, the load is rated between 2.7 volts to 3.3 volts, which requires a buck converter with a PI controller to keep the voltage within the operating voltage range. Finally, the battery will be charged based on the recommended profile, which means the controller will switch between CC and CV based on the battery SOC. However, the charging CC will depend mainly on the available power from renewable sources. On the other hand, the CV must be at 4.2 V, which means that the renewable sources will stop working at the MPP if the charging current becomes more than the rated capacity current of the li-ion battery. Therefore, the power management algorithm is shown in Fig. 1.28. It governs all the system variations for efficient battery charging and MPPT simultaneously. This algorithm also ensures a long-life term for the battery.

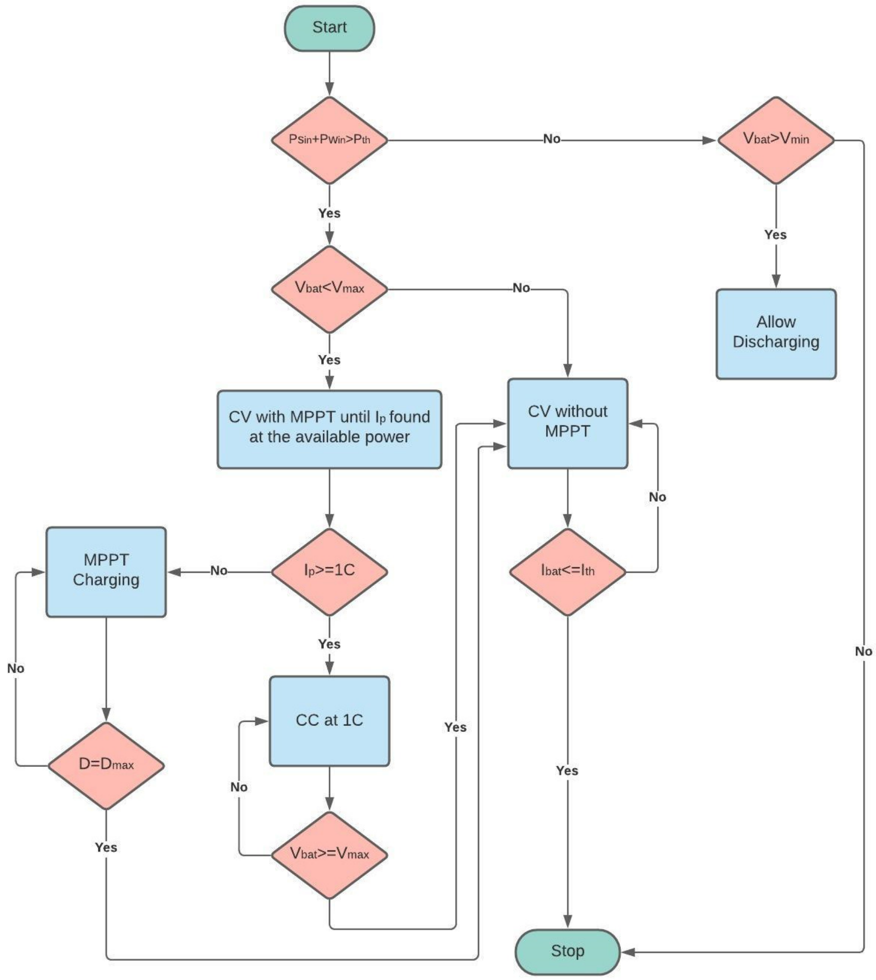

Figure 1.28: Power Management Flow Chart For battery charging based on MPPT.

1.8 Design Procedures

1.8.1 Renewable sources rating selection

Based on load, battery size, and surrounding environment, the renewable sources were chosen. For solar energy harvesting, a 3.5 W solar module with 6.5 peak voltage and 0.55 peak current at standard test conditions STD is sufficient for the application. Table 1.2 shows the solar module characteristic. Also, Fig 1.29 show the I-V and the P-V curves for this solar module at different irradiances and 25° C.

TABLE 1.2: SOLAR MODULE POWER SPECIFICATION

Specifications	Values

MC	12 cells
V_{oc}	7.7 V
V_p	6.5 V
I_{sc}	590 mA
I_p	550 mA
W_p	3.5 W
ζ %	19.1%

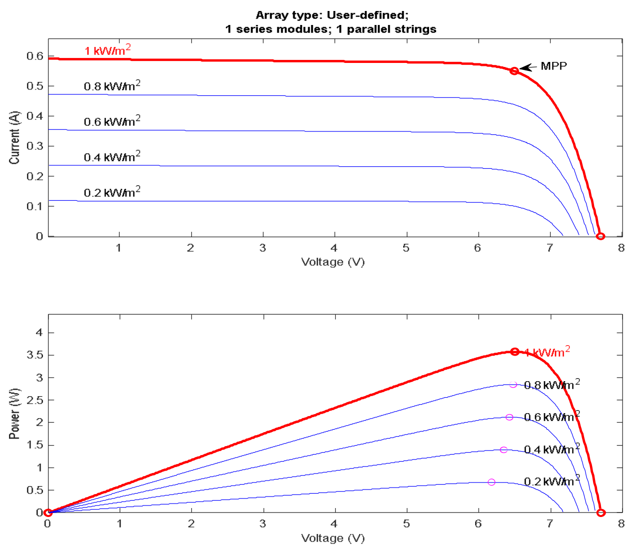

Figure 1.29: I-V and P-V characteristic curve of the chosen solar module at different irradiances and 25° C.

For wind energy harvesting, a 10 W with two propellers wind turbine has been chosen. The pitch angle is ten degrees for smooth and less vibration wind energy conversion. This angle is chosen due to the direct connection with the DC generator shaft. The wind turbine and the DC generator specifications are shown in Table 1.3, while the wind turbine characteristic curve is shown in Fig. 1.30.

TABLE 1.3: WIND TURBINE & PMDC MOTOR SPECIFICATIONS

Specifications	Values
# of Propellers	2
β (Pitch angle)	10°

Nominal P_m	10 W
PMDC motor P_o	15 W
[R_a (Ω), L_a (H)]	[0.15, 0.001]
K_t (N.m/A)	0.12
J (Kg.m^2)	0.0002

Where K_t is the torque constant, and **J** is the total inertia.

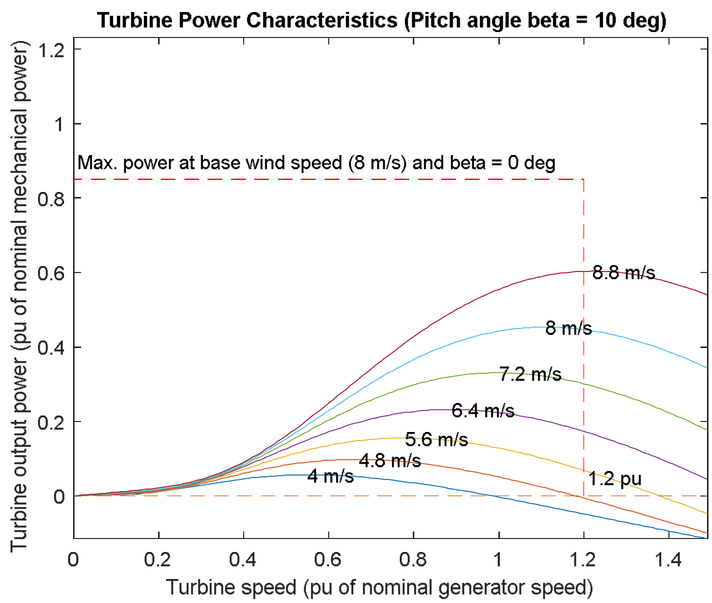

Figure 1.30: Turbine output power VS speed characteristic curves at different wind speed.

The vibration energy harvesting, piezoelectric strings were used. The output power of every single string is 25 mW, where multiple strings were connected in parallel. Two different types of forces were applied experimentally in the lab. The first type is the force applied to the bender (string) in both directions at low-frequency results in output voltage waveform, as shown in Fig 1.31. On the other hand, a hitting force is applied at the bender's tip to create a higher frequency waveform, as shown in Fig 1.32. However, due to the high price of a single unit of piezoelectric strings and the small amount of power, this report only investigates the vibration energy harvesting using simulation only.

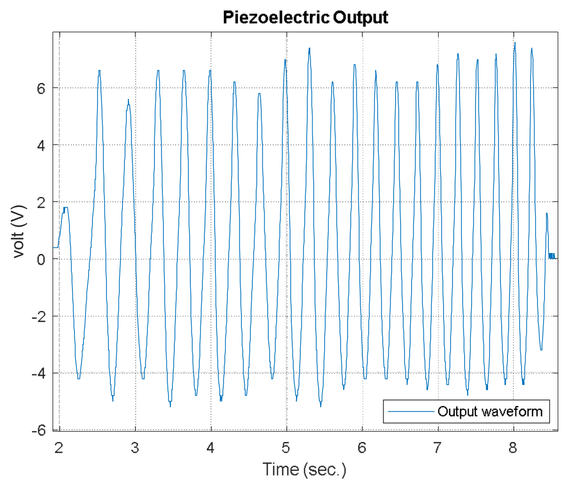

Figure 1.31: Output Voltage from the Piezoelectric string as bending force applied.

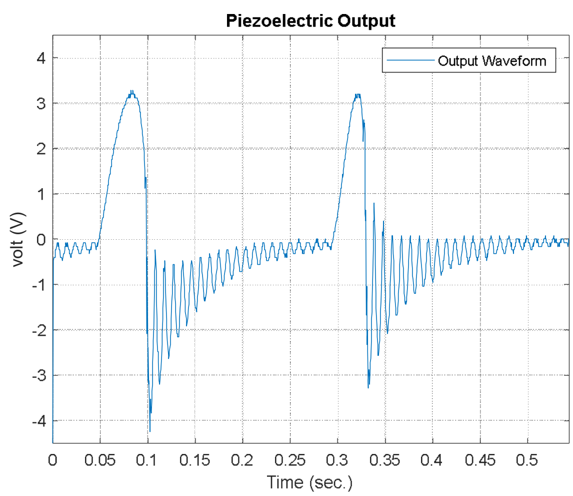

Figure 1.32: Output Voltage from the Piezoelectric string as vibrating force applied.

1.8.2 DC-DC converters Design Procedure

From Fig. 1.27, the buck-boost converter will drive the extraction from the solar module and pump it to the DC bus. Thus, the design requirement will depend on the source rating, desired output current, and the desired ripple. Therefore, Table 1.4 show all system specification plus the converter values used. Eqs. (1.23-1.26) and design procedures in [17] are used, where L and C have been chosen to be greater than the largest calculated value in both modes. Also, the battery bi-directional buck converter uses the same values for L and C.

TABLE 1.4: SOLAR MODULE CONVERTER DESIGN SPECIFICATIONS.

Specifications	Values
V_{in_max}	7.5 V
I_{in_max}	0.59 A
I_{out_max}	0.5 A
K_{ind}	30%
F_{sw}	20-100 kHz
ΔV_{out}	5-10%
L	120 uH
C_{out}	100 uF
C_{in}	10 uF

Furthermore, Table 1.5 represents the specifications for the buck converter used in the wind energy conversion. Eqs (1.17-1.19) and design procedures in [15] are used to calculate L and C values. Therefore, similar values were used for the load buck converter since the design output voltage (3 V) requires L and C values less than the chosen values for the wind buck converter.

TABLE 1.5: WIND TURBINE CONVERTER DESIGN SPECIFICATIONS.

Specifications	Values
V_{in_max}	12 V
I_{in_max}	1 A
I_{out_max}	0.5 A
K_{ind}	30%
F_{sw}	20-100 kHz

ΔV_{out}	5-10%
L	1000 uH
C_{out}	120 uF
C_{in}	10 uF

In addition, the vibration energy harvesting requires a low power diode full-bridge rectifier with an LC filter, where the energy is stored temporarily in a capacitor. After that, a buck converter is used to supply either the bus with a constant voltage of 4.2 V or the load with a constant voltage of 3 V for a very short time response. The buck converter's L and C values are chosen to be like the wind or the load buck converter. A buck converter is chosen because the capacitor will store energy equal to the capacitor's rated voltage. However, the energy must be released at 90% of the rated voltage to protect the capacitor from excessive charging. The excessive charging happens only in the simulation since the model uses a current source with a large shunt capacitor.

1.8.3 Linear controller design procedure for DC-DC converters.

The linear control theory and average linear modeling were discussed in sec 1.6.1. Therefore, the mathematical model in the Laplace domain (transfer function) for the buck converter is used to draw the bode plot for frequency analysis after substituting the values in table 1.4. this analysis will help design the controller when the buck-boost works in buck mode. Thus, the bode plot for the buck-boost converter when it operates in buck mode is shown in Fig. 1.33. from the bode plot, it is clear that the converter has an infinite gain margin and phase margin of 2.51° at 3.77 kHz. This phase margin is not sufficient to improve the responses of different system disturbances. Also, at low frequencies, the converter will suffer from steady-state error due to the constant gain value because it is a type-0 system. To improve the transient response and eliminate the steady-state error, a pole can be added by shifting the phase margin to a lower value [28].

The technique used to tune the PI controller is the stability boundary locus. The PI transfer function is shown in Eq (1.41). The converter's transfer function after substituting the specifications of table 1.4 is shown in Eq. (1.42). A lengthy derivation is done in [28] to get Ki and Kp of the PI controller as a function of phase margin and radian frequency as shown in Eqs (1.44-1.35).

$$G_c(S) = K_p + \frac{K_i}{S} \tag{1.41}$$

$$G_b = \frac{4.88 * 10^8}{S^2 + 900.9S + 7.508 * 10^7} \tag{1.42}$$

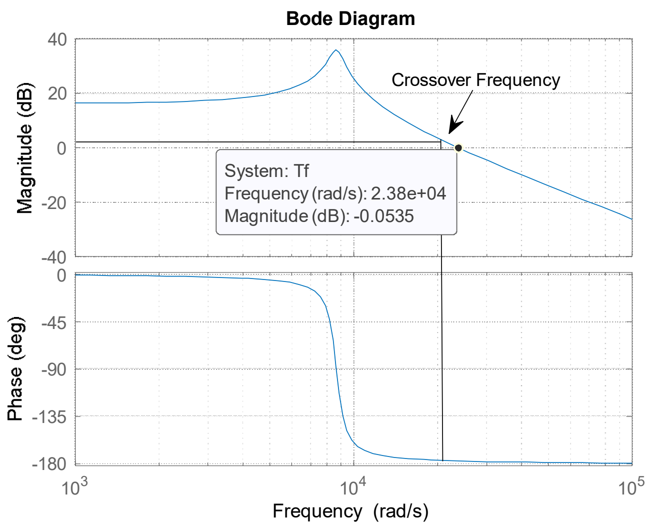

Figure 1.33: Bode plot for the buck-boost converter in buck mode.

$$G_b = \frac{b_0}{a_2S^2 + a_1S + a_0} \tag{1.43}$$

$$K_p(\varphi, \omega) = \frac{(-a_2b_0\cos(\varphi\omega^2) + a_1b_0\sin(\varphi\omega) + a_0b_0cos\varphi)}{-b_0^2} \tag{1.44}$$

$$K_i(\varphi, \omega) = \frac{\omega(a_2b_0\sin(\varphi\omega^2) - a_1b_0\cos(\varphi\omega) - a_0b_0sin\varphi}{-b_0^2} \tag{1.45}$$

Choosing the phase margin to angle around 60-75° will improve the system response and ensure stability. Therefore, substituting Eq (1.42) into Eqs. (1.44 &1.45) with varying, the frequency around the crossover frequency will draw the stability region, as shown in Fig 1.34. Thus, choosing any values for Kp and Ki will ensure stability due to achieving the desired phase margin.

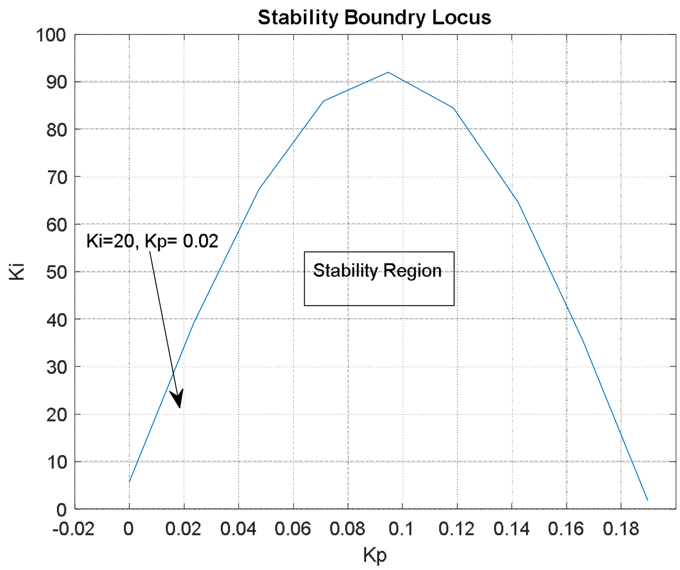

Figure 1.34: Stability Boundary locus for buck converter.

The procedure of designing a PI controller for the other DC-DC converters followed the same design procedure. However, the buck-boost converter will require to find the stability region and take the values of K_i and K_p within the common region (interact region). The Ki, and Kp for all the converters are shown in table 1.6.

TABLE 1.6: COMPENSATOR GAIN VALUES FOR THE DC-DC CONVERTERS.

Converter Type	K_i	K_p
Solar Buck-Boost	0.05	20
Wind Buck	0.005	60
Load Buck	0.005	60
Bidirectional Buck	0.02	20

1.8.4 Non-Linear controller design procedure.

Linear and non-linear controllers can be combined to increase the system's robustness and stability. Therefore, a non-linear controller as an inner loop control was designed for inductor ripple current compensation. However, the reference inductor current is calculated using a PI controller designed based on the previous section approach. Then, Bounding the reference inductor current by adding and subtracting it with a desired inductor ripple current. The maximum and the minimum boundaries compared to the instantaneous measured inductor current to create the control condition. This type of control is one of the sliding mode control techniques. Therefore, the system will slide on the desired ripple value tracking the average inductor current reference. This type of sliding mode control is called hysteresis switching control (HSC), and the PWM will be created based on the comparison results. Fig. 1.35 shows the controller block diagram, and the following equation illustrates the hysteresis switching concept.

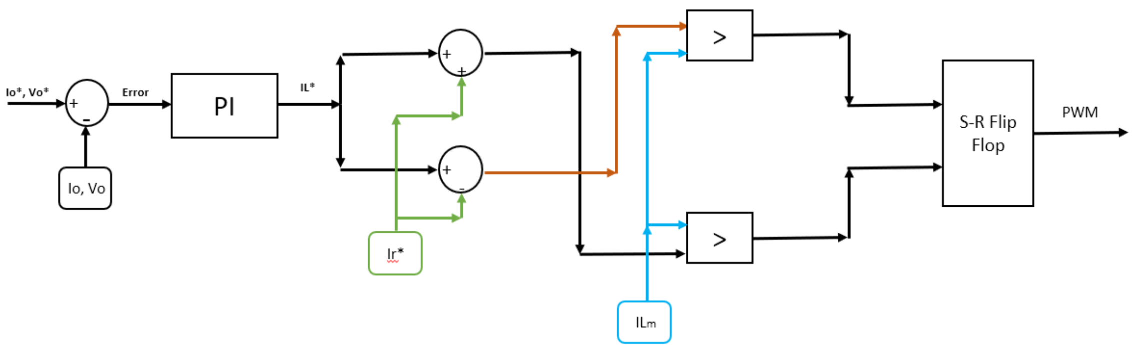

Figure 1.35: PI with hysteresis switching as inner inductor current controller.

a system with a state space equation x(t) that has bounded function |f(x)|<fo-constant could have the control signal u, where u is given by Eq (1.46)

$$u = \begin{cases} u_o & if\ i_L < I_L^* - \Delta i_r^* \\ -u_o & if\ i_L > I_L^* + \Delta i_r^* \end{cases} \tag{1.46}$$

i_L is the inductor current, and u_o is a constant depending on the system dynamic for switching operation such as the logic high and low. Also, the SMC could be represented mathematically as a relay control, as shown in Fig. 1.36. the condition for making the error reaches zero in a finite time is shown in (1.47).

$$i_L \dot{i_L} < I_L^* \tag{1.47}$$

The control signals for switch 1 or switch 2 based on the buck-boost operation mode is:

$$u_1 = u_2 = u = \frac{1}{2}(1 - sign(i_L)) \tag{1.48}$$

$$I_L^* + \Delta i_r^* < i_L \;\; Switch\ is\ OFF \tag{1.49}$$

$$I_L^* - \Delta i_r^* > i_L \;\; Switch\ is\ ON \tag{1.50}$$

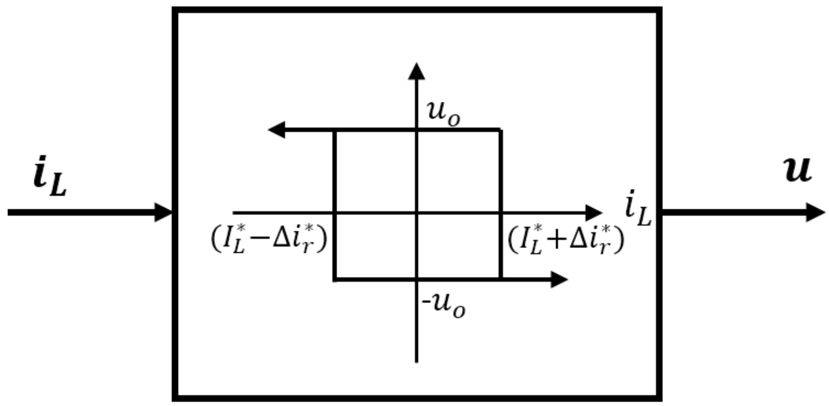

Figure 1.36: Sign Function (Relay Control)

Where u1 and u2 are the control signals of the two switches, respectively. Δir* is the desired ripple band of the inductor current. IL* is the desired average inductor current that has been calculated by the outer voltage or current controller loop (PI or PID). The hysteresis switching will happen when the actual inductor current is higher or lower than the boundary that is predetermined as the desired ripple. Therefore, if the inductor current is higher than the maximum desired inductor current value, the switch will turn off to start discharging. On the other hand, if the inductor is less, the switch will be turned on to start charging the inductor. However, if the actual inductor current between the boundary, the previous control signal will remain unchanged. Fig. 1.37 illustrate the methodology.

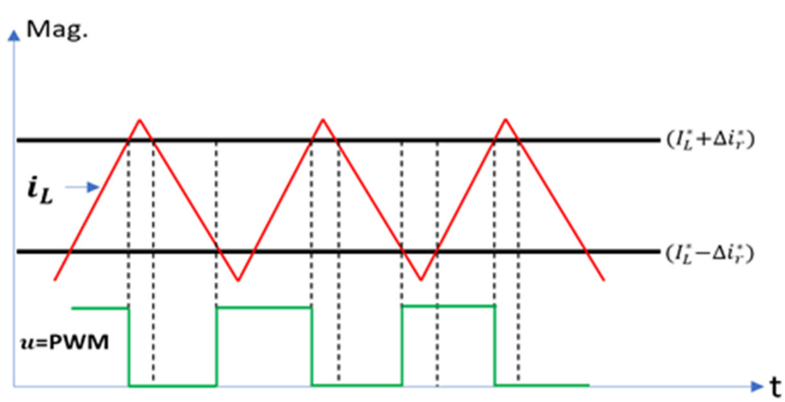

Figure 1.37: Hysteresis switching scheme.

Therefore, the reference output current or voltage can be calculated using one of the MPPT algorithms such as P&O and Incremental conductance. However, if this controller uses the MPPT algorithm, the system response will be driven by the MPPT response. For better resolution, the algorithm's step must be small, but the system will have a slower response.

The fuzzy controller is another non-linear controller technique where provides an alternative from designing controllers for complicated systems. Design fuzzy controller is done via heuristic information, in which a set of rules drive the system to perform as desired within the system's limitation. The fuzzy control sets of rules could come from extensive mathematical modeling, analysis, and control algorithm for a particular process. In more detail, the fuzzy will depend on making decisions based on various states between 0 and one compared to the conventional true and false [29]. Therefore, the decision of True will have a percentage of how possible that rule decision is True. The fuzzy logic block diagram is shown in Fig. 1.38.

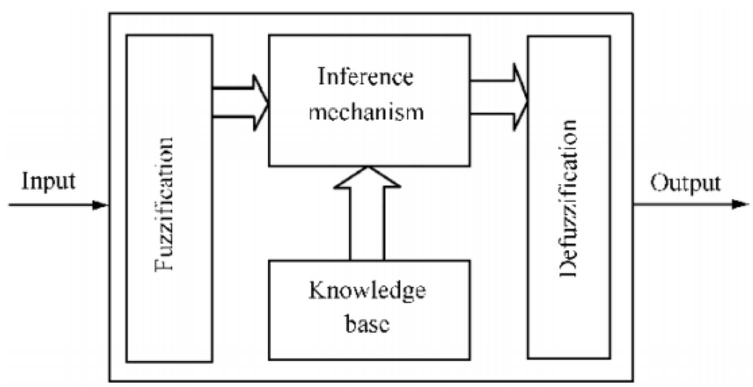

Figure 1.38: Fuzzy logic block [33].

From the fuzzy logic block diagram, the controller contains the following component:

a) The fuzzification interface that converts the crisp input values into fuzzy values
b) A knowledge base that contains an information about the application domain and control goals.
c) Decision-making logic performs interpretation for fuzzy control action, and it is called the inference mechanism.
d) The defuzzification interface converts the decisions from the inference mechanism into actual outputs.

Consequently, designing a closed-loop fuzzy logic controller for a DC-DC converter requires to understand the behavior of the converter based on the desired output or response. The block diagram for a closed-loop fuzzy logic controller is shown in Fig. 1.39. the error and the change of error is fed to the fuzzy input where the output is the duty cycle of the PWM signal that drives the DC-DC converter

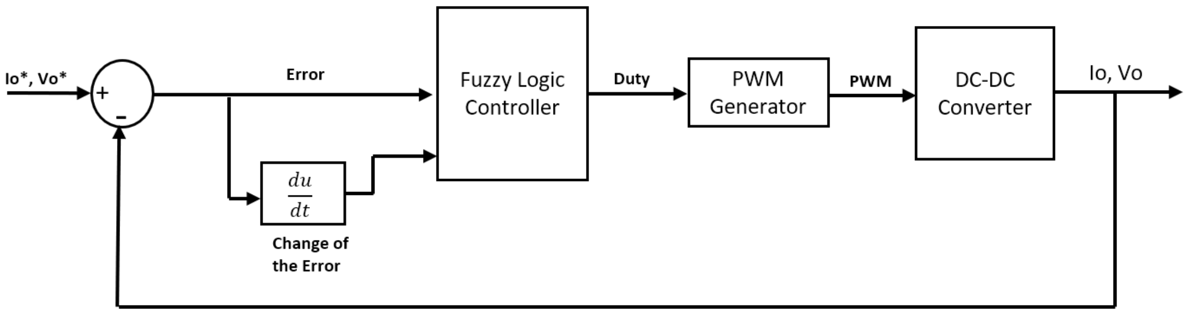

Figure 1.39: Closed loop fuzzy logic control for DC-DC converter.

FLC's fuzzification process creates crisp values from the two inputs by using membership functions built based on linguistic values. Thus, the calculated crisp values are fed into the inference mechanism for decision making. After that, the defuzzification converts the linguistic decisions into crisp control value using Eq. (1.51) and one of the two methods, the center of gravity method (COG) or the center average method (CA) as shown in Fig. (1.40) and Fig. (1.41) [33], respectively. For the DC-DC converters, the linguistic set of rules are shown in table 1.7, where 25 rules are created based on 7x7 linguistic values. The fuzzy system is shown in Fig. 1.42, while the membership functions for the error and change of error are shown in Fig. 1.43. Also, the output membership function is shown in Fig. 1.44.

$$u^{crisp} = \frac{\sum_i b_i \int \mu(i)}{\sum_i \int \mu(i)} \tag{1.51}$$

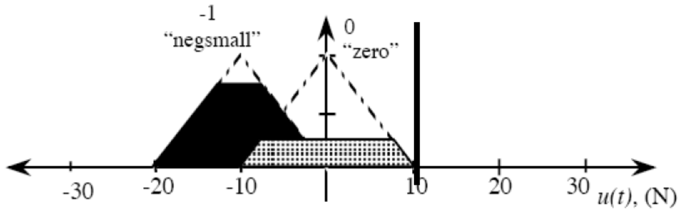

Figure 1.40: Center of gravity method [33].

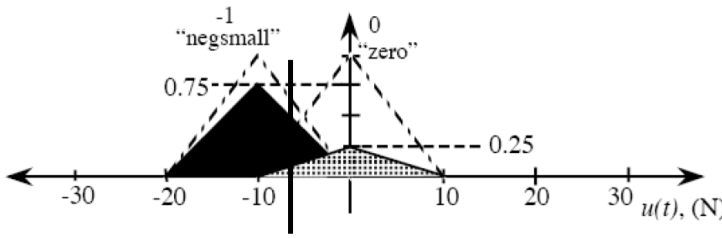

Figure 1.41: Center Average method [33].

Where:

i = 1,2

b1 = 0 from Fig. 1.39 & 1.40, b2= -10 from Fig. 1.39 & 1.40

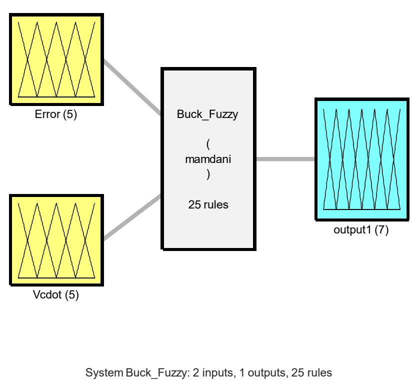

Figure 1.42: The FIS file of the fuzzy logic controller.

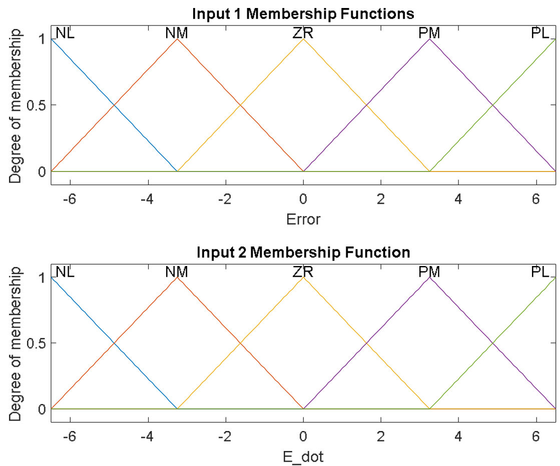

Figure 1.43: Error and Change of Error membership functions

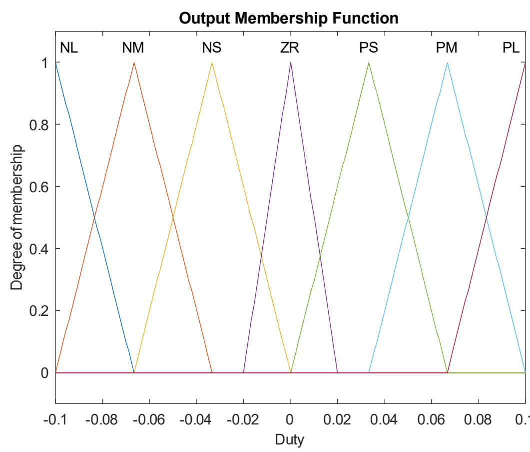

Figure 1.44: Output membership functions.

TABLE 1.7: SETS OF RULES FOR THE FUZZY LOGIC CONTROLLER.

Error / Change of Error	**NL**	**NM**	**NS**	**ZR**	**PS**	**PM**	**PL**
NL	NL	NL	NL	NM	NM	NS	ZR
NM	NL	NL	NM	NM	NS	ZR	PS
NS	NL	NM	NM	NS	ZR	PS	PM
ZR	NM	NM	NS	ZR	PS	PM	PM
PS	NM	NS	ZR	PS	PM	PM	PL
PM	NS	ZR	PS	PM	PM	PL	PL
PL	ZR	PS	PM	PM	PL	PL	PL

From the set of rules, the controller will have a significant effect on the error and error change due to the aggressive response from either direction (NL & PL). Also, the center rules have a line of zeros, which means that the error and the change of error are zero at that point. The control surface will give an overview of how the system should behave based on the rule set. Also, smoothing the output accomplished by reducing the rules that have a negative and positive large effect as shown in the control surface in Fig. 1.45.

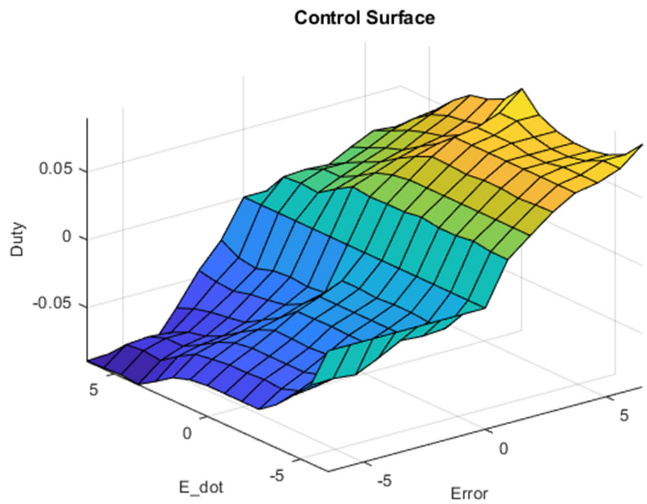

Figure 1.45: Control surface for the fuzzy logic controller.

Finally, the input has values equal to the maximum error and change of error possible, while the output has values ranging between -0.1 and 0.1. Therefore, this output is normalized and shifted between 0 and 1, which is the practical range of any PWM signal duty cycle. To achieve that, a summation with delayed feedback will adjust the fuzzy output to the range of 0 and 1. However, this is not the case, when the system reaches the instability point where it will keep adding the previous output of the fuzzy that have stopped at the maximum or the minimum output value. Thus, a limiter is added before the feedback point to bound the system between 0 and 1. This method is implemented, as shown in Fig. 1.46 in Sec. 1.9.